

# Direct-write waveplates using femtosecond lasers

**BEN McMILLEN,\* CHRISTOS ATHANASIOU, AND YVES BELLOUARD**

*Galatea Lab, STI/IMT, Ecole Polytechnique Fédérale de Lausanne (EPFL), Rue de la Maladière 71b, CH-2002, Neuchâtel, Switzerland*

*\*ben@mcmillen.eu*

**Abstract:** The use of femtosecond lasers to introduce controlled stress states has recently been demonstrated in silica glass. We use this principle in combination with chemical etching to demonstrate direct-write wave plates with precisely tailored retardance levels. In this work, we achieve sufficient retardance to act as a quarter-wave plate, producing a broadband device with a clear aperture free of any laser modifications. We analyze and model the stress distribution within the clear aperture, providing a generic template that can be applied to form multiple retardance levels within the same substrate.

**OCIS codes:** (140.390) Laser materials processing; (160.6030) Silica; (260.1440) Birefringence; (310.4925) Other properties (stress, chemical, etc.)

---

## References and links

1. K. M. Davis, K. Miura, N. Sugimoto, and K. Hirao, "Writing waveguides in glass with a femtosecond laser," *Opt. Lett.* **21**, 1729–1731 (1996).
2. K. Miura, J. Qiu, H. Inouye, T. Mitsuyu, and K. Hirao, "Photowritten optical waveguides in various glasses with ultrashort pulse laser," *Appl. Phys. Lett.* **71**, 3329–3331 (1997).
3. Y. Kondo, T. Suzuki, H. Inouye, K. Miura, T. Mitsuyu, and K. Hirao, "Three-Dimensional Microscopic Crystallization in Photosensitive Glass by Femtosecond Laser Pulses at Nonresonant Wavelength," *Jpn. J. Appl. Phys.* **37**, L94 (1998).
4. A. Marcinkevicius, S. Juodkazis, M. Watanabe, M. Miwa, S. Matsuo, H. Misawa, and J. Nishii, "Femtosecond laser-assisted three-dimensional microfabrication in silica," *Opt. Lett.* **26**, 277–279 (2001).
5. I. Y. Shimotsu, P. G. Kazansky, J. Qiu, and K. Hirao, "Self-Organized Nanogratings in Glass Irradiated by Ultrashort Light Pulses," *Phys. Rev. Lett.* **91**, 247405 (2003).
6. K. Minoshima, A. M. Kowalevich, I. Hartl, E. P. Ippen, and J. G. Fujimoto, "Photonic device fabrication in glass by use of nonlinear materials processing with a femtosecond laser oscillator," *Opt. Lett.* **26**, 1516–1518 (2001).
7. R. Osellame, S. Taccheo, G. Cerullo, M. Marangoni, D. Polli, R. Ramponi, P. Laporta, and S. De Silvestri, "Optical gain in Er-Yb doped waveguides fabricated by femtosecond laser pulses," *Electron. Lett.* **38**, 964–965 (2002).
8. H. Zhang, S. M. Eaton, J. Li, and P. R. Herman, "Type II femtosecond laser writing of Bragg grating waveguides in bulk glass," *Electron. Lett.* **42**, 1223–1224 (2006).
9. T. Meany, M. Gräfe, R. Heilmann, A. Perez-Leija, S. Gross, M. J. Steel, M. J. Withford, and A. Szameit, "Laser written circuits for quantum photonics: Laser written quantum circuits," *Laser Photonics Rev.* **9**, 363–384 (2015).
10. J. Tang, J. Lin, J. Song, Z. Fang, M. Wang, Y. Liao, L. Qiao, and Y. Cheng, "On-Chip Tuning of the Resonant Wavelength in a High-Q Microresonator Integrated with a Microheater," *Int. J. Optomechanics* **9**, 187–194 (2015).
11. Y. Bellouard, A. Said, M. Dugan, and P. Bado, "Monolithic three-dimensional integration of micro-fluidic channels and optical waveguides in fused silica," *MRS Proceedings*, **782**, 63–68 (2003).
12. Y. Cheng, K. Sugioka, and K. Midorikawa, "Microfluidic laser embedded in glass by three-dimensional femtosecond laser microprocessing," *Opt. Lett.* **29**, 2007–2009 (2004).
13. Y. Hanada, K. Sugioka, I. Shihira-Ishikawa, H. Kawano, A. Miyawaki, and K. Midorikawa, "3D microfluidic chips with integrated functional microelements fabricated by a femtosecond laser for studying the gliding mechanism of cyanobacteria," *Lab Chip* **11**, 2109–2115 (2011).
14. F. Bragheri, L. Ferrara, N. Bellini, K. C. Vishnubhatla, P. Minzioni, R. Ramponi, R. Osellame, and I. Cristiani, "Optofluidic chip for single cell trapping and stretching fabricated by a femtosecond," *J. Biophoton.* **3**, 234–243 (2010).
15. A. Schaap, Y. Bellouard, and T. Rohrlack, "Optofluidic lab-on-a-chip for rapid algae population screening," *Biomed. Opt. Express* **2**, 658–664 (2011).

16. Y. Bellouard, A. Said, and P. Bado, "Integrating optics and micro-mechanics in a single substrate: a step toward monolithic integration in fused silica," *Opt. Express* **13**, 6635–6644 (2005).
17. L. A. Fernandes, J. R. Grenier, J. S. Aitchison, and P. R. Herman, "Fiber optic stress-independent helical torsion sensor," *Opt. Lett.* **40**, 657 (2015).
18. B. Lenssen and Y. Bellouard, "Optically transparent glass micro-actuator fabricated by femtosecond laser exposure and chemical etching," *Appl. Phys. Lett.* **101**, 103503 (2012).
19. T. Yang and Y. Bellouard, "Monolithic transparent 3D dielectrophoretic micro-actuator fabricated by femtosecond laser," *J. Micromech. and Microeng.* **25**, 105009 (2015).
20. M. Beresna, M. Gecevičius, and P. G. Kazansky, "Polarization sensitive elements fabricated by femtosecond laser nanostructuring of glass [Invited]," *Opt. Mater. Express* **1**, 783–795 (2011).
21. M. Beresna, M. Gecevičius, P. G. Kazansky, and T. Gertus, "Radially polarized optical vortex converter created by femtosecond laser nanostructuring of glass," *Appl. Phys. Lett.* **98**, 201101–201101 (2011).
22. K. Mishchik, G. Cheng, G. Huo, I. M. Burakov, C. Mauclair, A. Mermillod-Blondin, A. Rosenfeld, Y. Ouerdane, A. Boukenter, O. Parriaux, and others, "Nanosize structural modifications with polarization functions in ultrafast laser irradiated bulk fused silica," *Opt. Express* **18**, 24809–24824 (2010).
23. Y. Bellouard, A. Champion, B. Lenssen, M. Matteucci, A. Schaap, M. Beresna, C. Corbari, M. Gecevičius, P. Kazansky, O. Chappuis, M. Kral, R. Clavel, F. Barrot, J.-M. Breguet, Y. Mabillard, S. Bottinelli, M. Hopper, C. Hoenninger, E. Mottay, J. Lopez, "The Femtoprint Project," *J. Laser Micro Nanoen.* **7**, 1–10 (2012).
24. A. Champion and Y. Bellouard, "Direct volume variation measurements in fused silica specimens exposed to femtosecond laser," *Opt. Mater. Express* **2**, 789–798 (2012).
25. A. Champion, M. Beresna, P. Kazansky, and Y. Bellouard, "Stress distribution around femtosecond laser affected zones: effect of nanogratings orientation," *Opt. Express* **21**, 24942–24951 (2013).
26. B. McMillen and Y. Bellouard, "On the anisotropy of stress-distribution induced in glasses and crystals by non-ablative femtosecond laser exposure," *Opt. Express* **23**, 86–100 (2015).
27. Y. Bellouard, A. Champion, B. McMillen, S. Mukherjee, R. Thomson, Y. Cheng, "Femtosecond laser-induced stress-state inversion and related anisotropies," *Optica*, under review (2016).
28. C.-E. Athanasiou and Y. Bellouard, "A Monolithic Micro-Tensile Tester for Investigating Silicon Dioxide Polymorph Micromechanics, Fabricated and Operated Using a Femtosecond Laser," *Micromachines* **6**, 1365–1386 (2015).
29. Y. Bellouard, "Non-contact sub-nanometer optical repositioning using femtosecond lasers," *Opt. Express* **23**, 29258 (2015).
30. Y. Bellouard, A. Said, M. Dugan, and P. Bado, "Fabrication of high-aspect ratio, micro-fluidic channels and tunnels using femtosecond laser pulses and chemical etching," *Opt. Express* **12**, 2120–2129 (2004).
31. OpenPolScope [computer software], (2015), <http://www.openpolscope.org>
32. S. Mehta, M. Shirbak, and R. Oldenbourg, "Polarized light imaging of birefringence and diattenuation at high resolution and high sensitivity," *J. Opt.* **15**, 094007 (2013).
33. S. Rajesh and Y. Bellouard, "Towards fast femtosecond laser micromachining of fused silica: The effect of deposited energy," *Optics Express* **18**, 21490–21497 (2010).
34. C.-E. Athanasiou and Y. Bellouard, "Investigation of the micro-mechanical properties of femtosecond laser-induced phases in amorphous silica," *Proc. SPIE* **9740**, 97401E (2016).
35. S. P. Timoshenko, J. N. Goodier, *Theory of Elasticity* (3<sup>rd</sup> ed.), (McGraw-Hill, 1970), Chap. 3, Sect. 24
36. F. Hecht, "New development in FreeFem++," *J. Numer. Math.* **20**, 251–266 (2012). <http://www.freefem.org>
37. A. K. Spilman and T. G. Brown, "Stress birefringent, space-variant wave plates for vortex illumination," *Appl. Optics* **46**, 61–66 (2007).
38. J. F. Nye, *Physical Properties of Crystals*, (Oxford University Press, 1985).
39. T. N. Vasudevan and R. S. Krishnan, "Dispersion of the stress-optic coefficient in glasses," *J. Phys. D Appl. Phys.* **5**, 2283 (1972).

---

## 1. Introduction: femtosecond laser writing as a tool to induce stress in silica

The effect of non-ablative ultrashort pulses on fused silica has been extensively studied over the last decade since the pioneering works that first demonstrated localized increase of refractive index [1,2], etching rate [3,4], and the occurrence of self-organized nanostructures [5]. These laser-induced modifications have been used in numerous applications, including integrated optics [1,6-10], optofluidics [11-15], optomechanics [16,17], actuators [18,19], and polarization optics [20-22], to name a few. A particular feature of this manufacturing process is that it can be implemented with compact, tabletop 3D printing systems [23].

Femtosecond laser exposure in the non-ablative regime induces a confined change of volume [24], creating oriented tensile or compressive stress fields capable of reaching locally high levels of stress (up to  $\sim 2$  GPa in compression) [25]. Interestingly, these laser-induced

stress fields can be tailored and controlled by changing the orientation of the laser polarization with respect to the writing direction [25,26], and by tuning the pulse duration of the laser [27]. This not only allows for control of the stress orientation, but also the magnitude and state, i.e. switching from tensile to compressive stress. This ability to fine-tune stress fields finds its origins in the variety of nanostructures induced in laser-modified materials, as highlighted in references [25-27]. This intriguing effect has already been applied to tensile testing procedures for investigating glass micromechanics [28], as well as for future concepts of optical component packaging [29].

Here, we explore the use of controlled stress-states for applications in polarization optics. Specifically, we present a technique for manufacturing polarization devices using the indirect action of laser-induced stress. Device geometry is defined using laser-machined silica substrates, limiting the action of the induced stress (and resulting birefringence) to a particular aperture. By using the same femtosecond laser for both machining and subsequent loading, the device manufacturing process can be greatly simplified.

## 2. Waveplate concept

The principle of a laser-machined waveplate is shown in Fig. 1. A rectangular clear aperture (labeled as zone c) is defined by two cuts made through a fused silica substrate using a wet-etch-assisted laser machining process [30]. After etching, a set of lines (which we call ‘stressors’) are machined in the bulk of the material at opposing ends of the rectangle (B), using writing parameters sufficient to generate nanogratings within the laser-affected zone [5]. These nanogratings are oriented parallel to the laser writing direction, such that the principal component of the stress tensor [25,26] is directed perpendicular to the line orientation.

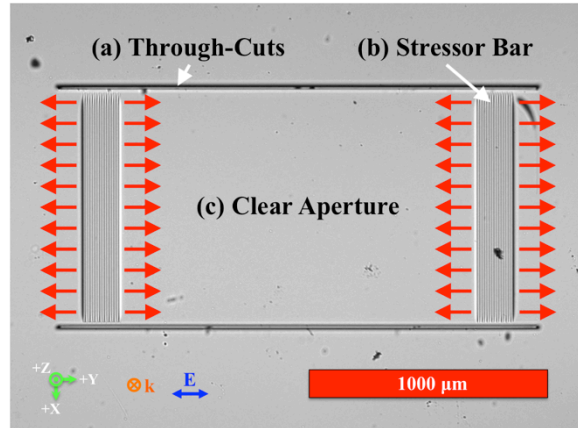


Fig. 1. Microscope image of a laser-machined waveplate. In this arrangement, a clear aperture (c) is defined by a pair of horizontal cuts (a), fabricated using a wet-etch-assisted laser machining process [30]. Stress-induced birefringence is then generated in this aperture by writing a set of vertical lines (labeled ‘stressor bar’, (b)) within the bulk of the substrate at each end of the device, using exposure conditions sufficient to generate nanogratings. Here, the writing polarization, and hence the orientation of the nanogratings, is chosen such that the generated stress behaves like a quasi-uniaxial loading, as indicated by the red arrows.

This arrangement of opposing stressors induces a quasi-uniaxial loading of the material in the center (as indicated by the red arrows in Fig. 1), generating a sizeable optical retardance within the clear aperture. With this simple arrangement, the cuts serve as a stress-free interface, confining the action of the stressors to the area of interest, in which the level of optical retardance can be tailored through careful control of the number, density, and exposure parameters of the stressors. It should be noted that, while the fabrication process

presented here is done in multiple steps, the action of machining and device loading could be combined prior to etching, simplifying the production process further.

### 3. Experimental procedure

#### 3.1 Setup and measurement principle

Waveplates were fabricated in several steps, beginning with the machining of 20 blank devices (no stressors, each device 1x2 mm, staggered on a 4 mm grid) in a 25x25x0.5 mm fused silica substrate, using an amplified femtosecond laser system (Yb-fiber, Amplitude Systèmes), delivering 280 fs pulses at 1030 nm. Following machining, the sample was etched in a 2.5% solution of hydrofluoric acid for ~ 8 hours. To maximize etch rate, the variable repetition rate of the laser was set to 760 kHz during machining (see reference [30]).

After etching, each device was loaded by progressively forming stressors composed of single layers of laser-modified material in the  $xy$  plane through the thickness of the sample ( $z$ -direction), with a plane pitch of 15  $\mu\text{m}$ . Individual lines in each plane were written perpendicular to the cuts of the device, evenly spaced along the  $y$ -direction (varied between 5 and 10  $\mu\text{m}$ ). The laser polarization was fixed perpendicular to each line in order to generate maximum stress along the long axis of the device ( $y$ -direction in Fig. 1).

Each group of stressors was embedded in the bulk of the substrate and spaced 20  $\mu\text{m}$  from all exterior surfaces to limit stress concentration and consequent crack formation. Additionally, each block was inset 100  $\mu\text{m}$  from the ends of the device. To ensure even loading, the repetition rate of the laser was reduced to ~ 80 kHz in order to maintain the required value of energy deposition for maximum stress, while keeping the writing velocity low, thereby limiting the influence of acceleration dynamics of the motion stages used during fabrication.

The resulting stress-induced birefringence was measured using a standard microscope (Olympus BX51) equipped with a liquid-crystal universal compensator for measuring birefringence (VariLC). The LC unit was controlled using freely available software (OpenPolScope [31-32]), which provided all the necessary functions for calibration of the LC compensator and retardance measurement acquisition. Further post-processing in MATLAB was then used to apply a false color-map to each measurement, as well as extract retardance data. For the purposes of this experiment, we only focus on the measured absolute retardance.

#### 3.2 Experimental results

We first examine the evolution of stress within the clear aperture of the waveplates as a function of deposited energy [33]. A pulse energy of 250 nJ was selected, and the speed varied from 1700 to 170  $\mu\text{m/s}$ , resulting in a deposited energy range of 10 to 100  $\text{J/mm}^2$ . The results of this experiment are shown in Fig. 2 below.

For this experiment, the line spacing of individual stressors was fixed at 10  $\mu\text{m}$ , with a total of 16 stressors per side (32 per device). From Fig. 2, the developed stress peaks around 20  $\text{J/mm}^2$ , giving a maximum retardance of just over 15 nm. Above this point, the retardance begins to decay, which we interpret as a consequence of stress-relaxation due to crack formation within the nanogratings. This measurement not only serves as a calibration to develop maximum stress during the writing process, but also confirms previous findings for stress evolution in the nanograting regime [24]. For reference, the phase shift at 546 nm (the wavelength used by the VariLC measurement system) is given on the right hand side of the graph.

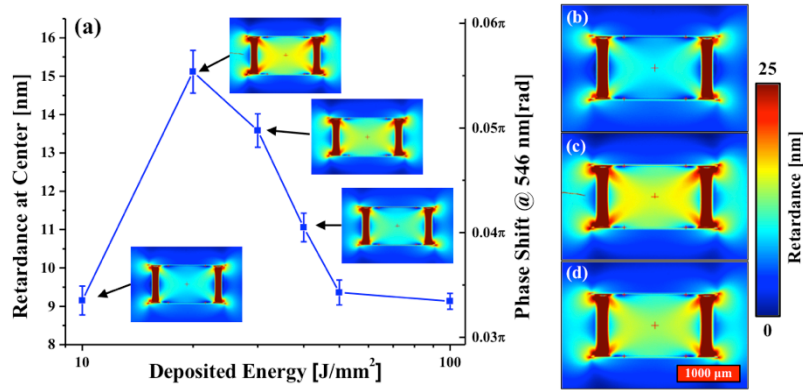


Fig. 2. (a) Retardance as a function of the energy deposited for a pulse energy of 250 nJ and a line spacing of 10  $\mu\text{m}$ . All devices were written with 16 stressors per side (32 stressors total per device). For these writing conditions, it was found that the stress peaks for a deposited energy of 20  $\text{J}/\text{mm}^2$ . The images in (b)-(d) show a magnified view of the retardance map for three waveplates spanning the range over the peak shown in (a), with deposited energy values of 10, 20, and 30  $\text{J}/\text{mm}^2$  respectively.

While the peak retardance developed in Fig. 2 is only on the order of  $\sim 15$  nm, this plot serves as a calibration for process control to determine the best writing conditions for generating stress in a single line. For further optimization of the developed stress, we now turn our attention to the lateral spacing of the stressors.

Based on the results shown in Fig. 2 (above), a deposited energy target of 20  $\text{J}/\text{mm}^2$  was chosen to fabricate three additional devices: one with a stressor spacing of 10  $\mu\text{m}$  and 64 total stressors, and two with a reduced spacing of 5  $\mu\text{m}$ , each with 64 and 128 total stressors respectively. The results are shown in Fig. 3 below. The device in Fig. 3(a) is the same displayed in Fig. 2(a), and is used as a reference (20  $\text{J}/\text{mm}^2$ ,  $\sim 15$  nm max retardance).

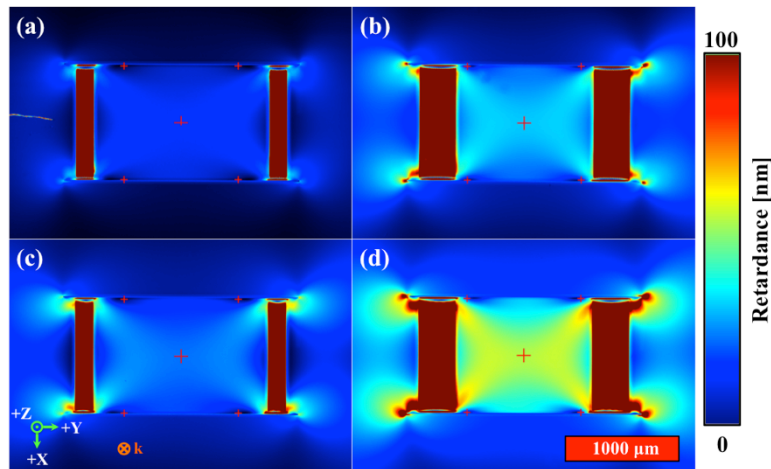


Fig. 3. Waveplate retardance as a function of the number of stressors and stressor spacing. (a) and (b) show retardance maps for a stressor spacing of 10  $\mu\text{m}$ , with 16 and 32 stressors per side, respectively. Devices (c) and (d) are similar, but for a stressor spacing of 5  $\mu\text{m}$  and 64 and 128 stressors per side, respectively. All devices were written with a deposited energy of 20  $\text{J}/\text{mm}^2$ , with the laser polarization fixed parallel to the long axis of each device. For comparison, the device shown in (a) has a peak center retardance of  $\sim 15$  nm, while the device in (b) is considerably higher at  $\sim 55$  nm.

Here we measure the developed retardance at the center of the clear aperture as a function of the spacing and number of lines in each stressor. Note that the retardance scale has a

maximum retardance of 100 nm. For the device shown in Fig. 3(d), a maximum retardance of  $\sim 55$  nm is developed. This retardance map will be used as a comparison and calibration for the following section on device modeling.

#### 4. Modeling and discussion

We now set out to describe the behavior of the developed stress in the waveplates in terms of a set of design parameters, such as the device geometry and the number and density of the stressors. These models may then be used as a set of design rules, giving full control over the stress field under different geometrical and loading conditions.

##### 4.1 One dimensional analytical model

As a first approximation, we consider a one-dimensional lumped model (illustrated in Fig. 4 below), following an approach reported in reference [28]. In this model, the modified and unmodified regions of the material are represented by springs, for which an equivalent stiffness may be derived.

In this model, the geometry of the waveplates is broken down into several distinct regions, as shown in Fig. 4(a). These regions are labeled as the volume between stressors, the laser-affected volume, the un-affected sidebars, and the clear aperture. Keeping with the spring-model approach, an equivalent stiffness is then specified for these regions, labeled in Fig. 4(c) as  $k$ ,  $k_2$ ,  $k_3$ , and  $k_w$  respectively.

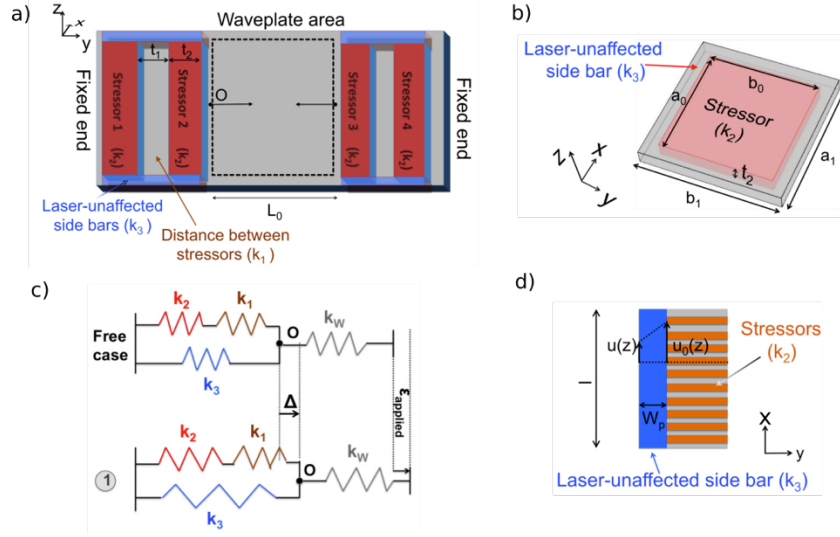


Fig. 4. (a) 2D visualization of the uniaxial loading process during stressor fabrication. (b) Parameters used to describe a single stressor. (c) Simplified spring model of the loading process. (d) Enlarged view of the shear stress development at the interface between the laser-affected and unaffected zones.

The model is then built by first starting with the region containing each stressor block, which is treated as a combination of two springs in parallel with a third, taking into account the composite nature of the stressors (consisting of affected and un-affected material, surrounded by pristine sidebars). This assembly is then placed in series with a fourth spring, representing the clear aperture.

It should be noted that this model is a simplification, as the interfacial energy between the various domains (laser-affected, pristine, etc.) is not considered. However, so long as we assume that the behavior of these regions is governed by linear elasticity, this approximation remains valid. Despite these subtleties, the mechanical behavior of the system is reasonably well predicted using this approach.

We begin by formulating the total stiffness of the system in terms of the number of stressors,  $n$ , which is given by the following equation (see Fig. 4(c) for reference):

$$\text{Stiffness} = \frac{2k_1k_2}{k_1+k_2} + 8k_3 + k_w \quad (1)$$

where the corresponding stiffness elements are given by:

$$k_1 = \frac{a_0b_0}{nt_1} E_{\text{SiO}_2}, \quad k_2 = \frac{a_0b_0}{nt_2} E_{\text{LAZ}}, \quad k_3 = \frac{(a_1b_1 - a_0b_0)}{(n-1)(t_1+t_2)} E_{\text{SiO}_2}, \quad \text{and} \quad k_w = \frac{(a_1b_1 - a_0b_0)}{L_w - 2n(t_1+t_2)} E_{\text{SiO}_2} \quad (2)$$

The quantities  $a_0$ ,  $b_0$ ,  $a_1$ , and  $a_2$  are the width and length of an individual stressor and surrounding material, respectively, while the quantities  $t_1$  and  $t_2$  correspond to the spacing between stressors (volume between stressors) and the stressor width (laser-affected volume).  $L_0$  is the initial length of the waveplate,  $E_{\text{LAZ}}$  is the elastic modulus of the laser-affected zones, and  $E_{\text{SiO}_2}$  is the elastic modulus of fused silica.

In addition to the simplifications mentioned previously in this section, we make the following assumptions:

1/ Fine structures within the laser-modified composite are ignored, and instead treated as a homogeneous material with a lower density than the surrounding, unmodified bulk. An average elastic modulus of 34 GPa was chosen for this region, which was recently reported in [28].

2/ For the particular arrangement of embedded stressors used here, a certain portion of the device loading is transferred to the bulk as shear stress; in this case along the regions label ‘unaffected sidebars’, as shown in Fig. 4(d). We consider this shear low and negligible, as calculated based the shear-lag model used in reference [28].

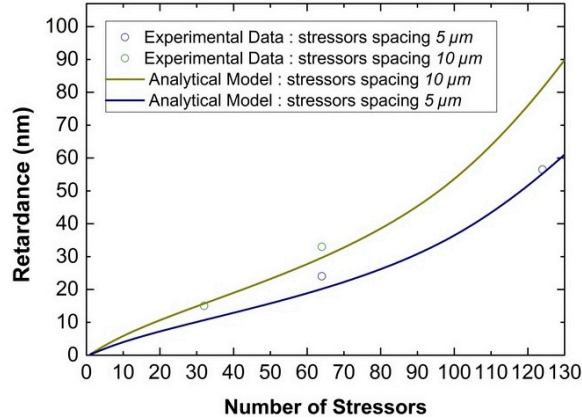


Fig. 5. Prediction of waveplate retardance as a function of the number and spacing of machined stressors using the 1D stiffness model outlined in section 4.1. Here, the circles represent the developed retardance in each waveplate (measured in the center of the clear aperture for each device shown in Fig. 3), while the curves are the predicted values based on the stiffness model. For each measured data point, the error was estimated from the standard deviation of the measured retardance over a  $1 \text{ mm}^2$  area of the clear aperture. This error however, is very small ( $<2 \text{ nm}$ ) and is therefore not visible on the graph.

Fig. 5 shows a comparison between the 1D model, and the measured values of retardance extracted from the center of the clear aperture for the devices shown in Fig. 3. Overall, the model is in good agreement for low and high numbers of stressors, however there is some deviation for intermediate numbers. While this model may serve as a good ‘first principles’ estimation, the accuracy it provides is limited, as we do not consider the 2D interaction of

stress present in the device. For an improved model, we now treat the full 2D structure, which we cover in the next section.

#### 4.2 Two-dimensional analytical model

While the simplified 1D model discussed in the previous section provides an adequate ‘first principles’ approach to predicting stress evolution from the number and density of machined stressors, it does little to describe the full contour of the induced retardance field. For analytical derivation of this full contour, we use a more refined model based on Airy stress functions [35]. In this model, the waveplate is treated as a two-dimensional body (finite rectangular domain) with a continuously distributed load along the width (provided by the action of the stressors), as depicted in Fig. 6.

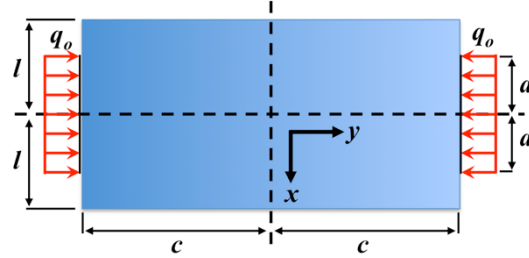


Fig. 6. Schematic representation of the loading case considered for the two-dimensional model. The terms here represent the dimensions of the waveplate ( $c$ ,  $l$ ), as well as the applied load ( $q_o$ ) and the area over which it is distributed ( $a$ ).

While a full derivation on the use of Airy stress functions is beyond the scope of this work, we will briefly outline the process here, referring to the notation used in Fig. 6. Here, we take assume a right-handed coordinate system, the origin of which is taken to be in the center of the rectangle defining the clear aperture. Following the work of Timoshenko [35], a general solution to the stress developed in the waveplate is found by defining a stress function  $\varphi(x,y)$ , which satisfies the biharmonic equation:

$$\frac{\partial^4 \varphi}{\partial x^4} + 2 \frac{\partial^4 \varphi}{\partial x^2 \partial y^2} + \frac{\partial^4 \varphi}{\partial y^4} = 0. \quad (3)$$

The equation  $\varphi(x,y)$  is of the form:

$$\varphi(x,y) = \sin \frac{m\pi x}{l} f(y) \quad (4)$$

where  $m$  is an integer, and  $y$  is the only independent variable of  $f(y)$ . Substituting eq. 4 into eq. 3, and making the substitution  $\alpha = m\pi/l$ , leads to the following equation for determining  $f(y)$ :

$$\sin(\alpha x) [f^4(y) - 2\alpha^2 f''(y) + \alpha^4 f(y)] = 0. \quad (5)$$

The stress function then becomes, after integration of eq. 5:

$$\varphi(x,y) = \sin(\alpha x) [C_1 \cosh(\alpha y) + C_2 \sinh(\alpha y) + C_3 y \cosh(\alpha y) + C_4 y \sinh(\alpha y)] \quad (6)$$

where the coefficients  $C_1 - C_4$  are computed using the boundary conditions of the substrate at the upper and lower edges ( $y = \pm c$ ). In order to accommodate generalized representations of the load applied to one edge of the substrate, a Fourier series is used, as follows:

$$q(x) = A_o + \sum_{m=1}^{\infty} A_m \sin(\alpha x) + \sum_{m=1}^{\infty} A'_m \cos(\alpha x), \quad (7)$$

with an additional loading term computed for the lower edge. For our case of symmetrical loading, the terms containing  $\sin(\alpha x)$  vanish from eq. 7, and the coefficients  $A_o$  and  $A'_m$  may be computed by:

$$A_o = \frac{q_o a}{l}, \quad A'_m = \frac{1}{l} \int_{-a}^a q_o \cos(\alpha x) \partial x = \frac{2q_o}{m\pi} \sin(\alpha a). \quad (8)$$

Here,  $A_o$  represents the uniform load applied to the right-hand edge. Finally, the 2D stress tensor is related to the stress function by:

$$\sigma_{xx} = \frac{\partial^2 \phi}{\partial y^2}, \quad \sigma_{yy} = \frac{\partial^2 \phi}{\partial x^2}, \quad \text{and} \quad \tau_{xy} = \frac{\partial^2 \phi}{\partial x \partial y} \quad (9)$$

where  $\sigma_{xx}$ ,  $\sigma_{yy}$ , and  $\tau_{xy}$  are the  $x$ ,  $y$ , and shear components of stress, respectively. Computing the derivatives of eq. 6, we arrive at the solutions that satisfy the biharmonic equation, giving a full tensorial description of the stress field in the clear aperture of the waveplate:

$$\begin{aligned} \sigma_{xx} &= \frac{q_o a}{l} + \frac{4q_o}{\pi} \sum_{m=1}^{\infty} \frac{\sin(\alpha a)}{m} \frac{\alpha c \operatorname{ch}(\alpha c) - \operatorname{sh}(\alpha c) \operatorname{ch}(\alpha y) - \alpha y \operatorname{sh}(\alpha y) \operatorname{ch}(\alpha c)}{\operatorname{sh}(2\alpha c) + 2\alpha c} \cos(\alpha x) \\ \sigma_{yy} &= -\frac{q_o a}{l} - \frac{4q_o}{\pi} \sum_{m=1}^{\infty} \frac{\sin(\alpha a)}{m} \frac{\alpha c \operatorname{ch}(\alpha c) + \operatorname{sh}(\alpha c) \operatorname{ch}(\alpha y) - \alpha y \operatorname{sh}(\alpha y) \operatorname{ch}(\alpha c)}{\operatorname{sh}(2\alpha c) + 2\alpha c} \cos(\alpha x) \\ \tau_{xy} &= \frac{q_o a}{l} + \frac{4q_o}{\pi} \sum_{m=1}^{\infty} \frac{\sin(\alpha a)}{m} \frac{\alpha c \operatorname{ch}(\alpha c) - \operatorname{sh}(\alpha c) \operatorname{ch}(\alpha c) \operatorname{sh}(\alpha c)}{\operatorname{sh}(2\alpha c) + 2\alpha c} \sin(\alpha x) \end{aligned} \quad (10)$$

with  $\alpha = \frac{m\pi}{l}$ ,  $ch = \cosh$ , and  $sh = \sinh$ .

Finally, using the stress components shown in eq. 10, the birefringence field was computed using the photoelastic relationships outlined in the Appendix.

In the next section, the performance of this model is compared with a finite element modeling (FEM) approach.

### 4.3 Finite element modeling

Finite element modeling was used as a means to verify the experimental results, as well as to provide an additional metric for comparison against the 2D analytical model discussed in the previous section. Of the many FEM software packages available, freeFEM++ [36] was chosen due to its low-level programmatic approach, giving a high degree of control over the modeling process.

The simulation domain was modeled after the peak device shown in Fig. 3(d) (maximum center retardance of  $\sim 55$  nm) using the displacement formulation [36]. As with the 1 and 2D analytical models, the stressors were treated as a homogeneous volume, and in this model, were represented as a rectangular region occupying the same area as the stressors of the original device. Furthermore, Dirichlet boundary conditions were used, specifying that all displacements must go to zero at the outer boundaries of the substrate. For this reason, the outer boundaries were grounded while all other boundaries internal to the domain were free to move.

In order to simulate the loading action of the stressors, an initial displacement was specified, directed along the long dimension of the device (see Fig. 1), for both lateral boundaries of each rectangle representing the stressor region. This value was computed by multiplying the stressor width (here approximately  $315 \mu\text{m}$ ) by a factor of 0.03%, the average unit strain for nanograting-induced stress (experimentally estimated in reference [24]).

Finally, stress-induced birefringence was calculated based on the photoelastic equation (outlined in the Annex), and the resulting field distribution was exported for processing in MATLAB. The results of this simulation are shown in Fig. 7, below.

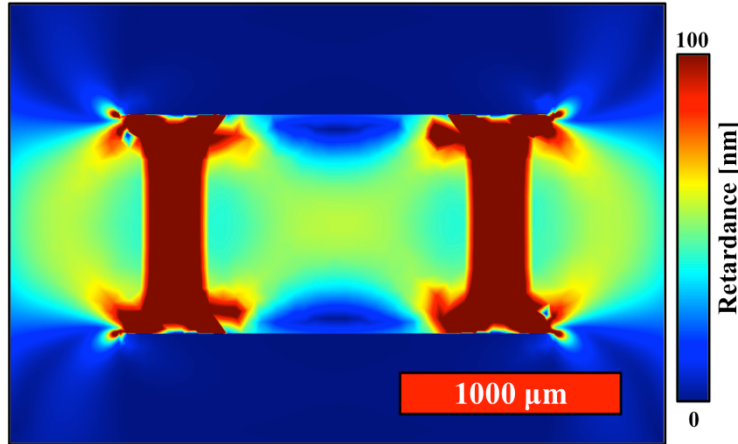


Fig. 7. Simulated retardance profile of a laser-written waveplate using a computed displacement on the boundaries of the stressors. The resulting average strain required to produce a maximum center retardance of 55 nm was  $\sim 0.16\%$ .

It should be noted that the value  $0.03\%$  is an *average* strain for nanograting-induced stress, and as we have done here, was computed by treating the composite region of the laser-modified material as homogeneous. As such, the resulting calculated retardance in the FEM model (when using this value) is under-estimated. To achieve a retardance value closely matching that of the original device, an iterative approach was used, gradually increasing the ‘virtual’ strain in the model until the desired retardance at the center of the clear aperture was achieved, resulting in a final value of  $\sim 0.16\%$ .

#### 4.3 Comparison with experimental results

Fig. 8 illustrates a comparison between experimental data, FEM simulation and the analytical model. Close to the homogeneous region in the middle of the waveplate, the two models matches well with the experimental data.

Qualitatively, both models explain the observed retardance in the clear aperture, however some discrepancies are evident near the boundaries. In the transverse profile (see Fig. 8), both the FEM and analytical models agree quite well, while the experimental data begins to diverge near the stressor regions. We suspect that this may be caused by a slight out-of-plane deformation, suggesting that the loading induced by the stressors requires further optimization. Indeed, no compensation for spherical aberration was used during the writing process. This can account for a decrease of localized intensity with increased writing depth, resulting in a slightly unequal distribution of stress across the substrate thickness. This stress gradient generates a net moment, and in turn favors out-of-plane bending. Such effects have been reported in previous work [28] and can be easily corrected, either by adjusting the power or the stressor spacing with respect to depth within the sample.

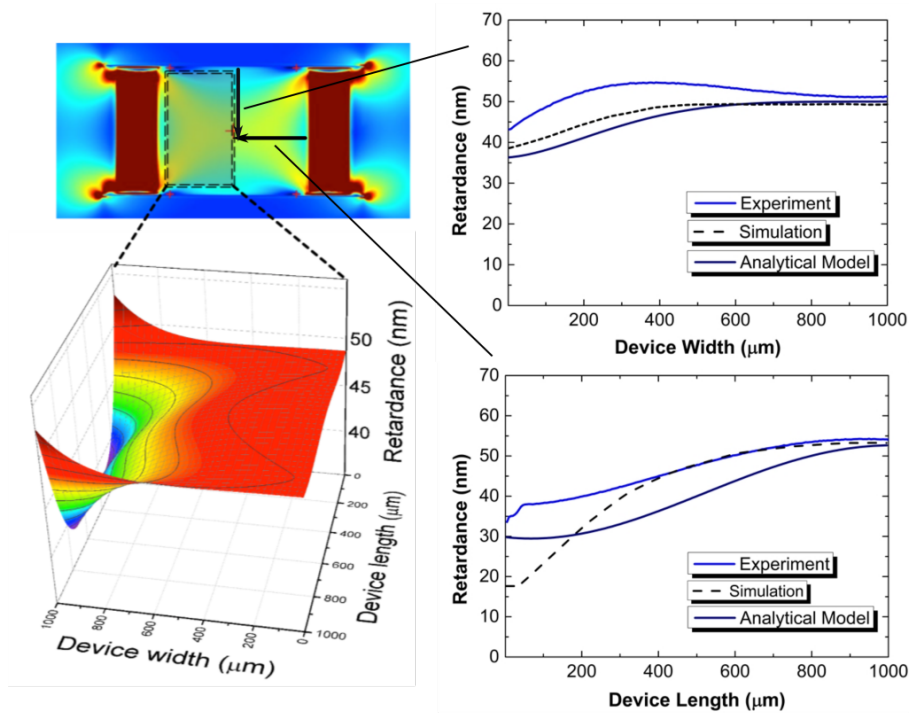


Fig. 8. Top-left: retardance map for the peak device shown in Fig. 3(d) (55 nm, 128 stressors, 5  $\mu\text{m}$  spacing). Bottom-left: 3D view of the retardance profile calculated using the 2D analytical model (only half the computed map is shown). Right: comparison between retardance data obtained for experimental measurements, FEM simulation, and the 2D analytical model. The inset at top-right shows a line profile taken at the middle of the waveplate along the vertical axis, while the bottom right illustrates the same data, but this time taken along the horizontal axis.

In the perpendicular direction, a similar effect can account for the differences in the observed trends, however an additional discrepancy is found between the analytical and FEM models. Here the FEM model predicts a lower retardance near the boundary. We attribute this effect to the fact that, in the FEM model the device is loaded using a prescribed displacement of the stressor interface, as opposed to a net stress.

## 5. Conclusion

This work demonstrates the use of direct-write femtosecond laser processing to induce predictable, controlled stress states within a chosen region of a substrate. Here, we utilize this technique to fabricate a polarization device, resulting in a simple waveplate. In this example, a basic geometry is used, consisting of a series of laser-written lines arranged in a perpendicular fashion, creating a rectangular region under uniaxial stress.

Though the results presented here are not fully optimized, we have provided a generalized framework, with which further development can be made. The flexibility of the direct-write process allows for virtually infinite combinations of cuts and stressors, opening up new design opportunities for more complex polarization devices. For example, one could consider devices based on two-dimensional stress states (as demonstrated by Spilman and Brown [37] at the macro-scale), leading to the creation of optical vortices. The technique we have introduced here allows for such a concept to be implemented at the micro-scale, and may be tailored to a variety of complex stress states.

## Acknowledgements

This work is supported by the European Research Council (ERC-2012-StG-307442, ‘Galatea’). The Galatea lab acknowledges the support of Richemont International. BMcM performed the experiments reported in this paper and the FEM modeling. CA derived the analytical models. YB proposed the concept of waveplates presented in this paper and supervised the research. All authors contributed to the writing.

## Annex: Photoelasticity and principal stress

The measured retardance is a result of a change in dielectric permittivity due to applied stress, and is given by [38]:

$$\zeta_{ij} = \pi_{ijkl} \sigma_{kl} \quad \text{where} \quad i, j, k, l = 1, 2, 3 \quad (11)$$

where  $\pi_{ijkl}$  is the fourth-rank piezo-optic tensor. Using Voigt notation, the tensorial equation in matrix form for a biaxial planar stress in an isotropic material becomes:

$$\zeta_{(1..6)} = \begin{bmatrix} \pi_{11} & \pi_{12} & \pi_{12} & 0 & 0 & 0 \\ \pi_{12} & \pi_{11} & \pi_{12} & 0 & 0 & 0 \\ \pi_{12} & \pi_{12} & \pi_{11} & 0 & 0 & 0 \\ 0 & 0 & 0 & \pi_{14} & 0 & 0 \\ 0 & 0 & 0 & 0 & \pi_{14} & 0 \\ 0 & 0 & 0 & 0 & 0 & \pi_{14} \end{bmatrix} \begin{bmatrix} \sigma_1 \\ \sigma_2 \\ 0 \\ 0 \\ 0 \\ 0 \end{bmatrix} = \begin{bmatrix} \pi_{11}\sigma_1 + \pi_{12}\sigma_2 \\ \pi_{12}\sigma_1 + \pi_{11}\sigma_2 \\ \pi_{12}\sigma_1 + \pi_{12}\sigma_2 \\ 0 \\ 0 \\ 0 \end{bmatrix} \quad (12)$$

where the birefringence ellipsoid ( $\Delta n$ ) view from the third axis (here the optical axis) is given in terms of  $\zeta$  as:

$$(\Delta n)_3 = \left| \left( n_o - \frac{n_o^3}{2} \zeta_1 \right) - \left( n_o - \frac{n_o^3}{2} \zeta_2 \right) \right| \quad (13)$$

or,

$$(\Delta n)_3 = \frac{n_o^3}{2} |(\sigma_2 - \sigma_1)(\pi_{11} - \pi_{12})| \quad (14)$$

and finally the retardance is given by:

$$R = C |\sigma_2 - \sigma_1| t \quad \text{and} \quad C = \frac{n_o^3}{2} (\pi_{11} - \pi_{12}) \quad (15)$$

where  $t$  is the thickness of the substrate, the value for  $C$ , the stress-optic coefficient for fused silica, is  $3.55 \cdot 10^{-12} \text{ Pa}^{-1}$  [39].

Note that the above equations rely on the principal stresses found in the substrate, which for the case of the FEM and 2D analytical models, must be computed from the  $x$ ,  $y$ , and shear stress components using the following relation:

$$\sigma_1, \sigma_2 = \frac{\sigma_{xx} + \sigma_{yy}}{2} \pm \sqrt{\left( \frac{\sigma_{xx} - \sigma_{yy}}{2} \right)^2 + \tau_{xy}^2} \quad (16)$$